Journal of Innovative Optical Health Sciences
Vol. 3, No. 4 (2010) 255–265

DOI: 10.1142/S1793545810001131

World Scientific
www.worldscientific.com

RETINAL SPECTRAL IMAGING AND BLOOD FLOW MEASUREMENT

PAUL LEMAILLET*, DONALD D. DUNCAN†, ART LOMPADO‡, MOHAMED IBRAHIM§, QUAN DONG NGUYEN§ and JESSICA C. RAMELLA-ROMAN*,‖

*Department of Biomedical Engineering
The Catholic University of America
620 Michigan Ave., N.E., Washington, DC 20064, USA

†ECE Department, Portland State University
1900 SW Fourth Avenue, Portland, OR 97201, USA

‡Polaris Sensor Technologies, 200 Westside Square Suite 320
Huntsville, AL 35801, USA

§Wilmer Eye Institute, Johns Hopkins University
Baltimore, MD 21287, USA

¶lemaillet@cua.edu

‖ramella@cua.edu

Measurement of both oxygen saturation and blood flow in the retinal vessels has proved to give important information about the eye health and the onset of eye pathologies such as diabetic retinopathy. In this study, we present the implementation, on a commercially available fundus camera, of a retinal imager and a retina blood flow velocimeter. The retinal imager uses division of aperture to acquire nine wavelength-dependent sub-images of the retina. Careful consideration is taken to improve image transfer by measuring the optical properties of the fundus camera and modeling the optical train in Zemax. This part of the setup is calibrated with optical phantoms of known optical properties that are also used to build a lookup table (LUT) linking phantom optical properties to measured reflectance. The retina blood flow velocimeter relies on tracking clusters of erythrocytes and uses a fast acquisition camera attached to a zoom lens, with a green illumination LED-engine. Calibration is provided using a calibrated quartz capillary tube and human blood at a known flow rate. Optical properties of liquid phantoms are retrieved from measured reflectance using the LUT, and blood flow measurements in the retina are presented.

Keywords: Retinal oximetry; fundus ophthalmoscope; multi-aperture camera; blood flow velocity; diabetic retinopathy.

1. Introduction

Diabetic Retinopathy (DR) is a common disease that can lead diabetic patient to blindness. However, the risk of visual loss can be reduced by early detection and treatment.[1] Since diabetic retinopathy has been linked to the oxygen saturation values in the retina vessels,[2] this metric is essential in monitoring DR progress. Kohner *et al.*[3] also showed that retina vessel blood flow and auto-regulation changes are linked to the onset of diabetic retinopathy. Hence, non-invasive measurements of both the oxygen saturation and the blood flow in retina vessels

is highly desirable. Calculation of oxygen saturation relies on the hemoglobin absorbance spectrum and can be accomplished by spectrometric measurements of the light reflected from the patient fundus. However, the complex structure of the eye fundus as well as the saccadic eye movements add to the complexity of blood velocity measurements and retinal imaging. Snapshot acquisition of spectrally diverse images can help oxygen saturation assessment. Hence, our group previously proposed a six wavelengths oximeter using a lens array and a filter array to project six wavelength-dependent images on a large CCD.[4] Various designs of retinal oximeter were proposed over the years[5–8] but retinal oximeters are still at a research stage.

Assessment of retina vessels blood flow can be accomplished with Laser Doppler Velocimetry (LDV),[9–11] a modality based on the Doppler effect. LDV is based on the detection of the frequency shift between an incident wave and the wave bouncing off a moving object; the resulting shift is related to the velocity of the object. Laser Speckle Velocimetry (LSV) has also been used to monitor red blood cells motion in the retina.[12,13] Movements tend to blur the speckle pattern and measurement of speckle contrast or loss of correlation can then be used for quantification of motion.[14]

In this paper, we present the implementation, on a commercially available fundus ophthalmoscope, of both a retinal blood velocimeter and spectral imager. The spatial division of the fundus image is obtained by a lenslet array that projects nine sub-images on a digital camera. A filter array, laying between the lenslet array and the CCD, provides wavelength selection. The effects of the eye movements are minimized by the simultaneous acquisition of spectrally different sub-images. Focusing on the eye region of interest is provided by a zoom lens coupled to a fast acquisition camera which replaces the original eyepiece of the fundus ophthalmoscope. This optical train, coupled to a green illuminating source replacing the bulb of the original fundus camera, is also used to track the retinal vessel red blood cells to estimate the blood flow velocity. The retinal imaging part of the setup is calibrated with a set of solid phantoms matching the absorption coefficient and the reduced scattering coefficient expected from eye reflectance measurements. The calibration of the blood velocimeter uses a calibrated quartz capillary positioned at the fundus of an eye phantom, and a calibrated syringe pump that pushes human blood in the capillary. Spectral images of three liquid phantoms of known optical properties combining human hemoglobin and calibrated microspheres were taken. The absorption coefficients and scattering coefficients of the liquid phantoms were extracted from the measured reflectances by using a lookup table computed first from reflectance measurements of the calibration phantoms. Blood velocity results in the eye are also presented.

2. Materials and Methods

Our experimental setup is based on a commercially available fundus ophthalmoscope (Carl Zeiss, Jena, Germany) onto which were implemented a blood velocimeter and a spectral imager.

2.1. *Retinal blood velocimeter*

Our approach to assess blood flow is related to tracking the red blood cells. The high absorption of both oxy- and deoxy-hemoglobin in the green region of the spectrum allows for high contrast imaging of retinal blood vessels. Hence, a LED-based light engine (λ = 525 nm, 15 nm FWHM, Enfis, Swansea, UK) replaced the original focusing light source of the ophthalmoscope. The original eyepiece was replaced by a fast acquisition camera (8-bit BW CCD, 60 Hz, Dalsa Genie, Billerica, MA) attached to a zoom lens (f = 150–450 mm, $f/\#$ = 5.6–32, Computar, Commack, NY). The LED-engine was connected to the camera strobe port. A train of programmatically controlled illuminating pulses was used for blood flow assessment. The strobe duration had a minimum of 3 μs but was increased to 6 μs with a 0.5 μs strobe delay during the blood flow measurements. Both camera and light engine were controlled through a custom-made software and user interface (MATLAB, Natick, MA). Four seconds of images were captured for the flow analysis, and all images were saved in an uncompressed AVI format.

2.2. *Spectral imager*

2.2.1. *Optical design*

The purpose of the oximeter part of the setup was (1) to achieve spatial division of the fundus image, and (2) to have the sub-images fill a large CCD (Lumenera 12-bit monochromatic digital camera, 35 mm × 23 mm, 4,008 pixels × 2,672 pixels, North Andover, MA, USA). Our former experimental

setup relied on off-the-shelf small diameter lenses (Sunex, $f \approx 6\,\text{mm}$), relaying the fundus ophthalmoscope image obtained on a focusing screen.[4] Unfortunately, the image quality tends to decrease because of the screen and as a result, so does the resulting oxygen saturation measurement precision. The modification of the optical design was intended to improve the light collection efficiency, for increased signal-to-noise ratio images, and to optimize the output imagery by minimizing aberrations and maximizing the sub-images size and spatial resolution. The design was constrained by (1) the optical characteristics of light exiting the Zeiss fundus camera, and (2) practical considerations such as the number of desired sub-images and the size of the CCD. The light exiting the fundus camera produces an exterior image whose position and diameter were measured. It was also experimentally determined that the exit beam was telecentric, with its optical pupil positioned at infinity. This image was therefore modeled in Zemax as a telecentric object, to be re-imaged into a 3×3 array of sub-images at the CCD. Mapping the entire object field into each sub-image requires that the division of aperture lens array lies in an optical pupil plane. The lens array extent is constrained by the CCD size which therefore sets the required pupil diameter. A set of re-imaging achromats was used to relocate the optical pupil to a position where the lens array could be placed and set the pupil diameter slightly larger than lens array to maximize optical efficiency. The array lens focal lengths were derived from the required magnification. An optical ray trace of the completed system is shown in Fig. 1. The slow nature of the resulting train is a result of the high $f/\#$ and telecentricity of the fundus camera, which result in a very low optical (Lagrange) invariant. Each resulting sub-image at the CCD plane is 8.0 mm in diameter, covering a full field of view of 30°. Two-fold mirrors are used to make the system more compact.

Figure 2(a) shows a cross-section of the train at the pupil plane schematic superimposed by the CCD at the image plane (dashed rectangle). Each 4 mm diameter array lens has an associated 5 mm square spectral filter, resulting in nine quasi-monochromatic sub-images at the CCD. The array lenses fit just within the pupil diameter, represented

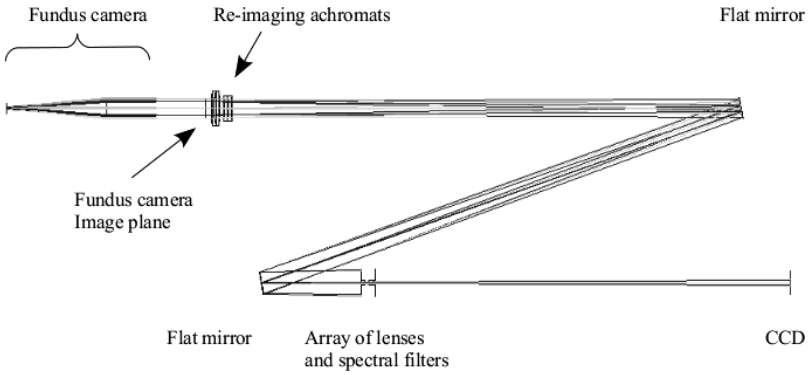

Fig. 1. Optical ray trace of the division of aperture optical train.

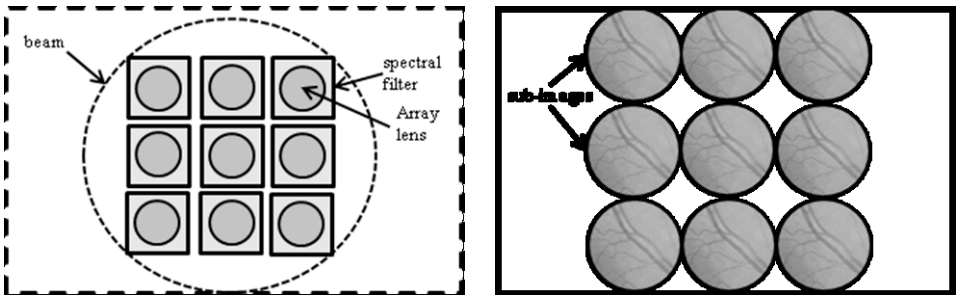

(a) (b)

Fig. 2. (a) Cross-section of pupil plane showing array lens and spectral filter arrangement. (b) Image plane cross-section showing sub-image arrangement.

by the dotted circle. Figure 2(b) shows the CCD plane cross-section and the arrangement of the sub-images. The slow nature of the system presented an easy optimization problem in terms of minimizing aberrations. The worst monochromatic offender was distortion with a Seidel coefficient of 0.68 waves, which equated to less than 0.5% at full field. Longitudinal chromatic aberration was small but non-negligible. The chromatic focal shift envelope across the operating waveband was ≈870 μm, which, in the slowly converging image space, does not cause noticeable defocus. Also, the individual array lenses could be displaced axially within the array mount to correct this error if needed.

Since the geometrical optics modeling does not account for diffraction, a physical optics model was also evaluated. This is very important for such a slow system since figures of merit such as the point spread function (PSF) and attainable spatial resolution are driven by diffraction effects. The calculated PSF diameter was ≈100 μm ($1/e^2$ point), or about 11 pixels. Figure 3 shows the encircled energy for a point image as a function of the collection radius.

One should note that the response is virtually independent of object field angle, and a similar weak dependence on wavelength was found. Although the imaged point size is relatively large, the system is seen to be operating at the diffraction limit. Figure 4 shows the systems modulation transfer function which indicates good spatial resolution up to 12.5 cycles/mm ($1/e^2$ point) again across the entire object field and all wavelengths.

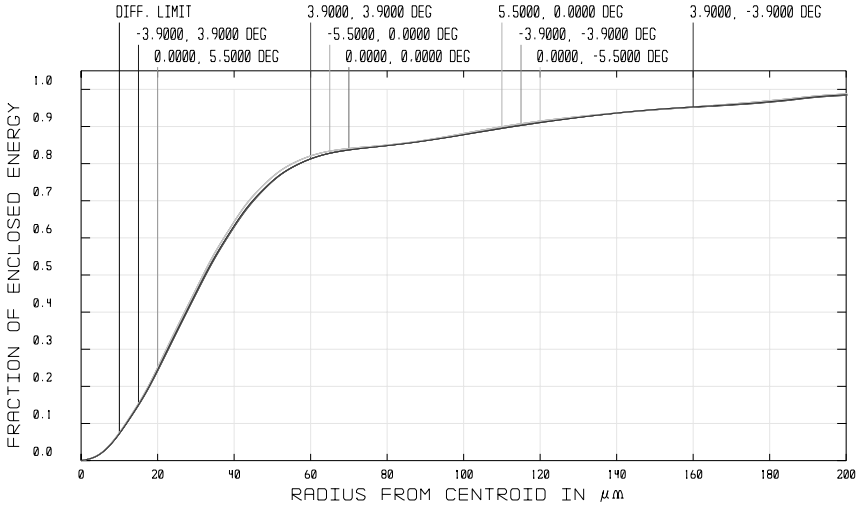

Fig. 3. Encircled energy for single image point across full field of view.

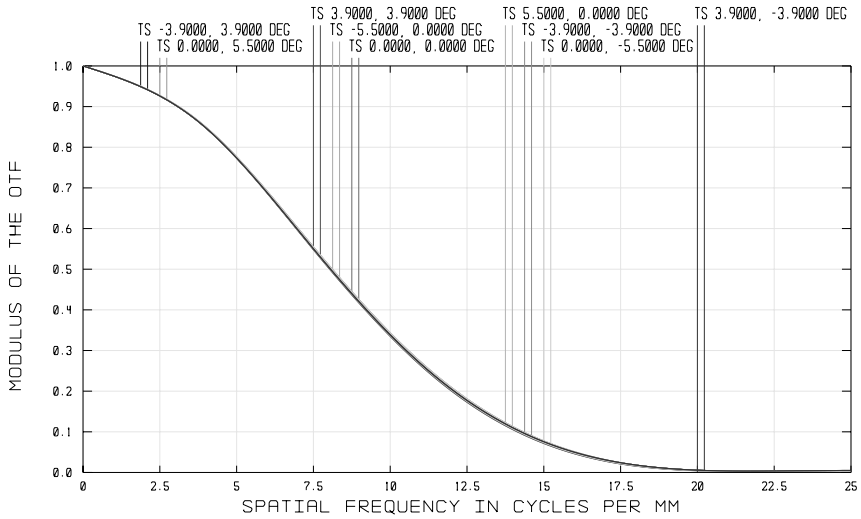

Fig. 4. Modulation transfer function shows good spatial resolution up to 12.5 lp/mm ($1/e^2$ point).

2.2.2. *Technical realization*

Figure 5 illustrates the technical realization of the retinal imager part of the setup and its optimized optical train. The image plane of the fundus ophthalmoscope is re-imaged by an achromatic doublet (L1, converging lens, $f = 140$ mm, and L2, diverging lens, $f = -150$ mm). The resulting beam is then spread through the filter array for spectral division of the sub-images. Those sub-images are obtained by an array of nine achromats ($f = 300$ mm).

One should remember that (1) the chosen focal length is derived from the desired image resolution, and (2) the CCD size imposes small diameter lenses. Both conditions, i.e., large focal length and small diameter, are not reached by off-the-shelf lenses. Hence, commercially available lenses were edged down to achieve the desired diameter. Position adjustment of the lens array and the CCD was greatly eased by using an eye phantom recently built by our group[15] which reproduces the eye structure as well as the fundus optical properties. This helped locating the eye fundus to be imaged by the optical train. Instead of being 5 mm square, available off-the-shelf narrow band filters (10 nm FWHM, Newport, Irvine, CA, USA) were 6 mm square to 8 mm square. The choice of filter wavelengths, i.e., 540, 550, 560, 580, 610, 630, 640, 650 and 670 nm, was guided by previous publication,[16,17] Monte Carlo simulations of light travel into retinal tissues, as well as commercial availability. Longer wavelength filters (600–700 nm range) were included in the filter array

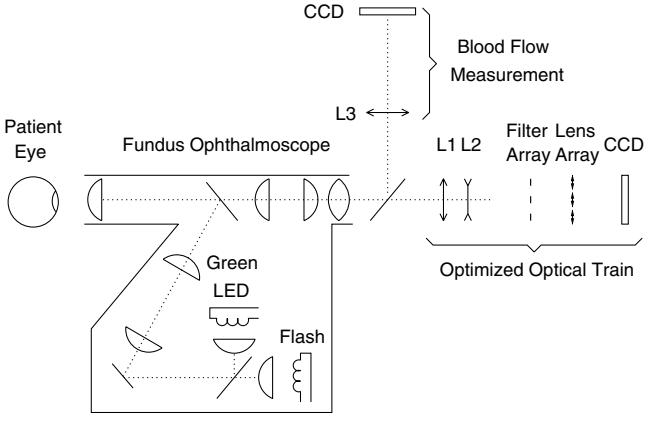

Fig. 5. Experimental setup: L1, converging lens ($f = 140$ mm); L2, diverging lens ($f = -150$ mm). The array lenses have a $f = 300$ mm focal length, and a 6-mm diameter (edged down off-the-shelf lenses). The blood velocimetry part of the setup is composed of a fast acquisition camera and a zoom lens L3 ($f = 150$–450 mm, $f/\# = 5.6$-32).

so as to help establish melanin concentration.[18] Then, absorbance effects of melanin can be extrapolated for lower wavelengths and subtracted from the overall absorbance. Shorter wavelength sub-images are used to fit oxy- and deoxy-hemoglobin absorption curves and assess the oxygen saturation in the retina. Owing to the strong absorption of the eye, and specifically melanin, a strong illumination is required. Hence, the flash is the light source used for oximetry measurements. However, focusing on the fundus area of interest is provided by the blood flow velocity measurement part of the system, i.e., green illumination and a fast acquisition camera. During focusing and positioning of the system, the strobe duration was reduced to 3.0 μs for the comfort of the patient and the camera gain was set to the maximum. For focusing, image acquisition for oximetry measurements and blood flow measurements, the maximum permissible exposure, MPE, was measured to be well below the maximum values allowed by ANSI Z136.1.

2.3. *Image registration*

2.3.1. *Blood flow velocimeter*

The clinical assessment of blood velocity in the retina vessel is achieved by dilating the patient eye with 1% tropicamide and 2.5% phenylephrine eye drops. Fixation of the undilated eye helps to minimize voluntary eye movements but saccadic eye movements are unfortunately inevitable; hence we select only sequence of images between major saccades and we register each frame using a two-step rigid-body translation. The first step is based on a correlation matching and achieves registration to the nearest pixel. The subsequent registration, based on a gradient technique,[19–21] registers to a sub-pixel precision. A region displaying several vessels is necessary to achieve good registration. From the registered set of images, a mean image is computed and displayed to the analyst.

2.3.2. *Spectral imager*

In order to better simulate the conditions of the image acquisition with a patient eye, we located a 1951 USAF Resolution Target (Edmunds Optics Inc., Barrington, NJ) at the fundus of the eye phantom, which was filled with purified water to simulate the eye vitreous humor. Figure 6 presents the nine sub-images of the USAF target with no filter array,

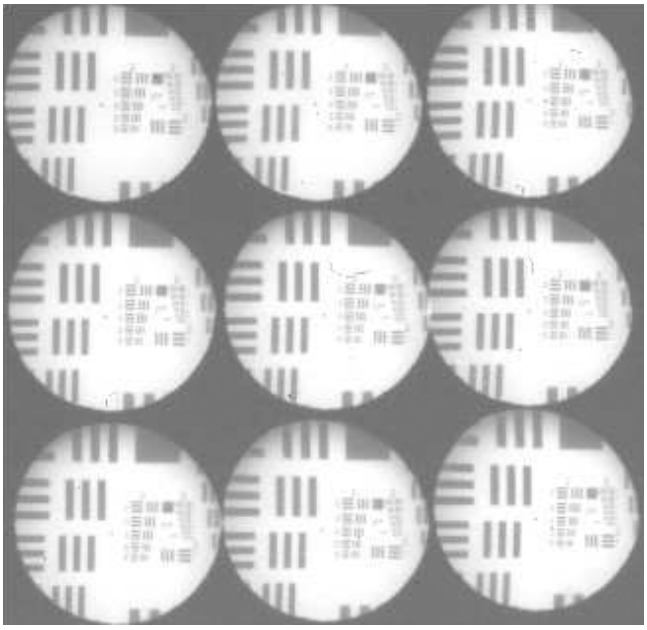

Fig. 6. Nine sub-images of the USAF target with no wavelength selection (i.e., no filter array). The registration of the images is done manually by choosing a common area of interest.

i.e., no wavelength selection. The registration of the images is done manually by choosing a common area of interest. This procedure gives the coordinates of equivalent areas in each of the nine sub-images and these coordinates are further used to register the *in vivo* images of the eye fundus.

2.4. *Calibration of the setup*

2.4.1. *Blood flow measurements*

The blood velocimeter was calibrated using a quartz capillary (inner diameter 165 μm) positioned at the fundus of the eye phantom.[15] Human blood was pumped through the capillary by a calibrated syringe pump (Hamilton, Reno, NV), at different adjustable rates (50 to several hundreds of μl/h). The centerline of the capillary image was defined and the gray level was extracted along this line for each image. These traces were stacked in a spatio-temporal matrix called a trace history. Processing of this trace history to calculate absolute blood velocity is as follows: an estimate of the illumination is formed by taking the outer product of the row averages and the column averages of the trace history. The residual (difference between the illumination and trace history) matrix displays a subtle tilted corrugation pattern that is associated with the motion of the inhomogeneous distribution of RBCs. This pattern arises because a group of RBCs appears at one point along the vessel, and in a subsequent image frame at a different point along the vessel. One needs to only estimate the tilt of the structure to determine the blood flow velocity. This estimate is made by taking a Radon transform of the residual image. The peak in the transform is at the angular orientation of the corrugations. The necessary calibration factors are the image frame sample interval and the pixel size. Details are provided in Duncan *et al.*[22]

2.4.2. *Spectral imaging*

The retinal oximeter was calibrated using a set of 30 calibration phantoms of various μ_a and μ_s' values. These phantoms were built by another group[23] and are composed of polyurethane as a casting material, titanium dioxide as a scattering agent and ink as an absorbing agent. Two shapes of phantoms were available, cylinders (diameter = 62 mm, height = 86 mm), as well as slabs (diameter = 60 mm, thickness = 2 mm). The calibration phantoms were designed so that their absorption coefficient (μ_a) and reduced scattering coefficient (μ_s') match a specific μ_a-*vs*-μ_s' grid. Optical properties were measured for λ = [350–850] nm, with an integrating sphere and Inverse Adding Doubling (IAD).[24] Figure 7 presents the μ_a-*vs*-μ_s' grid for a specific wavelength value λ = 632.5 nm. A picture of the actual phantom grid is presented in Fig. 8. The cylindrical phantoms were set in a mechanical housing made of polycarbonate walls (width = 78 mm, height = 72 mm, depth = 140 mm) simulating the eyeball. Similarly to our eye phantom,[15] a small hole (6 mm diameter) in front of the mechanical housing simulates the pupil of the eye and a plano-convex lens (f = 17 mm, Rolyn Optics, Coviana, CA) was positioned in front of the pupil to mimic the crystalline lens. Again, the housing was filled with purified water to simulate the vitreous humor.

Images of the cylindrical phantoms were taken, using the flash as the illuminating source, and the diffuse reflectance values were calculated using Eq. (1):

$$R = A \times \frac{I_{\text{Phantom}} - I_{\text{dark}}}{I_{\text{Standard}} - I_{\text{dark}}}, \tag{1}$$

where A is a scaling factor accounting for the setup apparatus. The intensity reflected from

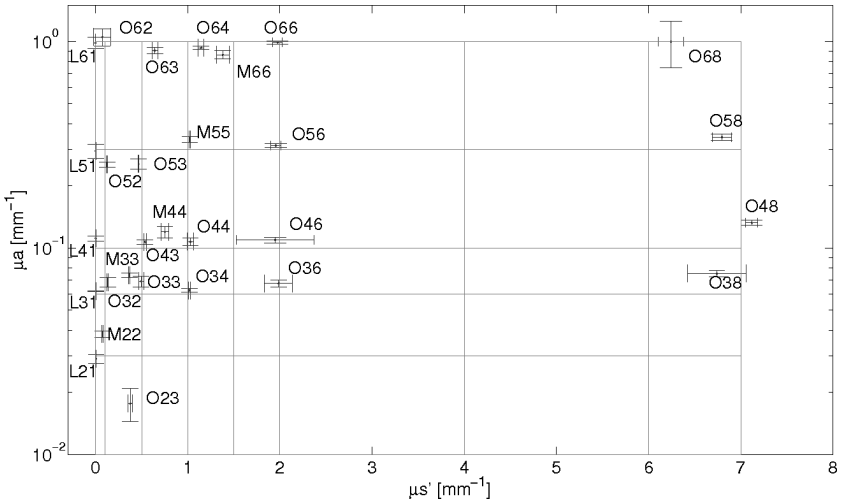

Fig. 7. Absorption coefficient (μ_a) and reduced scattering coefficient (μ_s') grid for the calibration phantoms at $\lambda = 632.5$ nm.

Fig. 8. Picture of the phantom grid. Absorption coefficient μ_a increases from bottom row to top row whereas reduced scattering coefficient μ_s' increases from left column to right column.

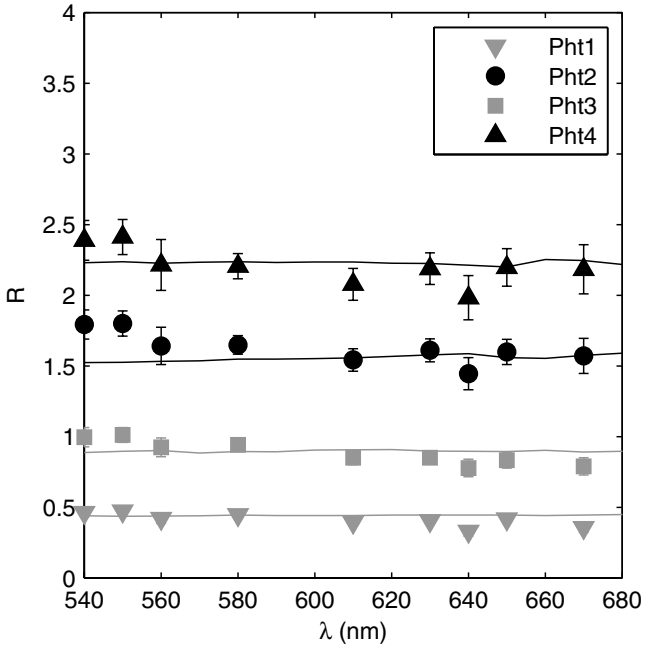

Fig. 9. Reflectance measurements of nine wavelength-dependent snapshot images (filled symbols) and comparison to Monte Carlo simulations (lines) for four of the calibration phantoms.

the eye phantom, I_{Phantom}, is normalized by the intensity reflected from a 60% reflectance standard (Labsphere, North Sutton, NH), I_{Standard}. A dark image was also captured, keeping the light source off. This image was subtracted from every image.

We compared the measured reflectance to the computed ones based on Monte Carlo simulations (MCML,[25] one million photons). An incident pencil beam was set at eight different wavelengths, distributed between 450 nm and 700 nm. Values of μ_a and μ_s' from IAD computations as well as a scattering anisotropy of $g = 0.5$ were used for these simulations. Results presented in Fig. 9 show for a set of four phantoms that the measured reflectance is close to Monte Carlo simulations.

3. Results

We first present blood flow measurement results in the eye. After selection of region of interest of the fundus image (Fig. 10), a center region is selected. A short segment of vessel is then selected, its centerline determined as well as the vessel

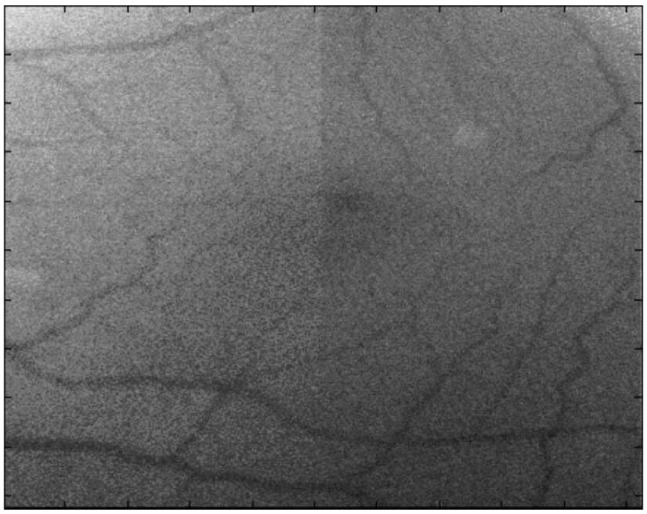

Fig. 10. A single frame used for the reconstruction of flow in the retina.

walls. The analysis described in Ref. 22 is run and the blood flow value is derived from the analysis. Resulting values of the venous (V) and arterial (A) blood flow are displayed in mm/s (Fig. 11).

The purpose of the retina imager is to assess the optical properties of the retina as a prerequisite to the estimation of the oxygen saturation in the retinal vessels. The relationship between R, μ_a and μ_s' is complex and a lookup table (LUT) was computed to estimate the optical properties of a medium from the measured reflectance values.[26]

To build the LUT, the measured reflectances were associated with the measured optical properties of the calibration phantoms. Next, R, μ_a and μ_s' were interpolated to a grid of uniformly spaced values of μ_a and μ_s', as illustrated in Fig. 12. To test the retrieval of the optical properties from the measured diffuse reflectance, a set of liquid phantoms were built, with 100% oxygenated human hemoglobin as an absorber (ferrous stabilized hemoglobin powder mixed with deionized water; Sigma, St. Louis, Missouri) and polystyrene microspheres as a scatterer (diameter 0.5 μm; Polysciences, Warrington, Pennsylvania). We used Mie theory to calculate $\mu_s'^{\text{Mie}}$ for the microspheres and a spectrometer to measure μ_a^{Spec} of a stock Hb solution (20 mg/ml). We created three liquid phantoms with $\mu_s' = [0.75, 1.25, 1.5]\ \text{mm}^{-1}$ at $\lambda = 630$ nm and a Hb concentration of 0.787 mg/ml ($\mu_a = 0.17\ \text{mm}^{-1}$ at $\lambda = 576$ nm). Extraction of the optical properties used a nonlinear fitting routing with two proportionality parameters (A, B) for μ_a^{Spec} and $\mu_s'^{\text{Mie}}$, respectively, and one (C) for R, the last one accounting for collection efficiency of the optical system. The optimization procedure started with a set of A, B and C parameters values, computed $\mu_a^{\text{calc}} = A \times \mu_a^{\text{Spec}}$ and $\mu_s'^{\text{calc}} = B \times \mu_s'^{\text{Mie}}$ and used the LUT to obtain a calculated value of the reflectance, R^{calc}. The measured reflectance, R^{meas}, is compared to the calculated one and the error

$$err = \sum_{\lambda} (R^{\text{calc}} - R^{\text{meas}})^2, \tag{2}$$

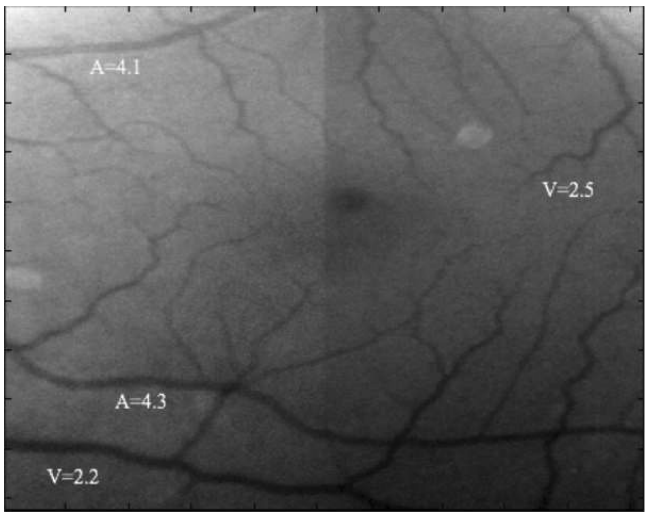

Fig. 11. Final fundus image obtained averaging 14 different registered frames. Flow velocities for venules (V) and arteries (A) are in mm/sec.

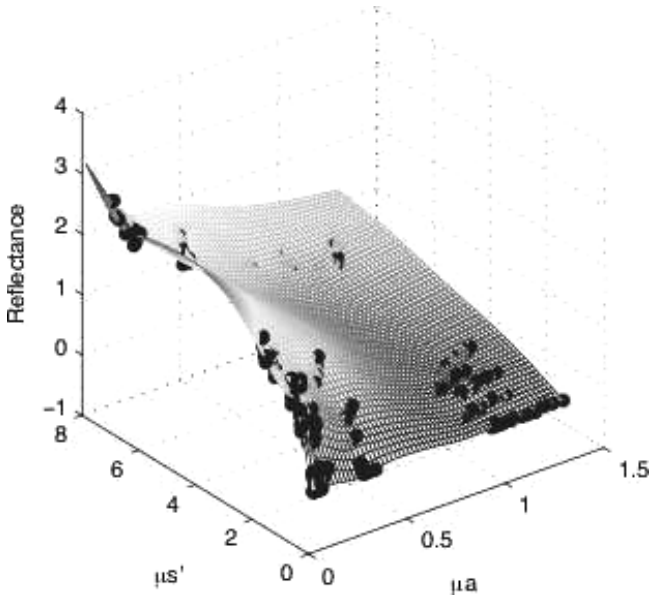

Fig. 12. Lookup table (LUT) extrapolated from the reflectance measurements and the μ_a and μ_s' values of the phantoms.

is minimized to assess the A, B and C values and consequently $\mu_a^{\mathrm{Pht}}(\lambda)$ and $\mu_s'^{\mathrm{Pht}}(\lambda)$ of the phantom.

The absorption coefficient of hemoglobin above 600 nm is so small that it was barely measurable with our spectrometer. This led us to limit the optimization procedure to the shorter available wavelengths, i.e., $\lambda = [540, 540, 550, 560, 580\,\mathrm{nm}]$, and further extend the results to the nine original wavelengths once A and B were estimated. Figure 13 illustrates the good agreement between the calculated values of $\mu_s'^{\mathrm{Pht}}(\lambda)$ compared to the expected ones based on Mie theory.

Figure 14 presents the calculated values of $\mu_a^{\mathrm{Pht}}(\lambda)$ compared to the expected ones based on the spectrometric measurements of the absorption coefficient, showing a reasonable agreement. What appears to be a better agreement at higher wavelengths is actually caused by the low absorption of hemoglobin at these wavelengths.

One should note that starting parameters in the nonlinear routine are the key parameters to a good extraction of the optical parameters, even in the ideal scenario we put ourselves into, i.e., the estimation of the optical parameters of the phantoms when scattering coefficient is known. The absorption coefficient can be expressed in terms of oxygen saturation, S, as

$$\mu_a = S\mu_a^{\mathrm{Hb\,Oxy}} + (1 - S)\mu_a^{\mathrm{Hb\,Deoxy}}, \qquad (3)$$

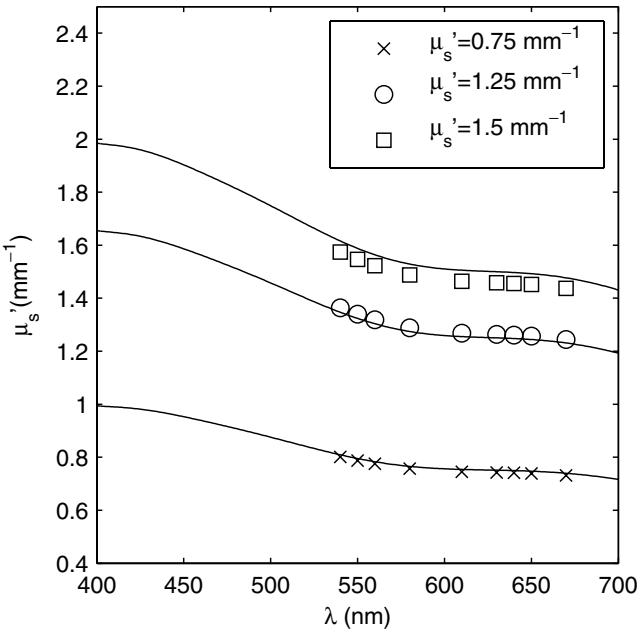

Fig. 13. Comparison of the measured (symbol) and expected (solid) reduced scattering coefficient versus wavelength for the three liquid phantoms.

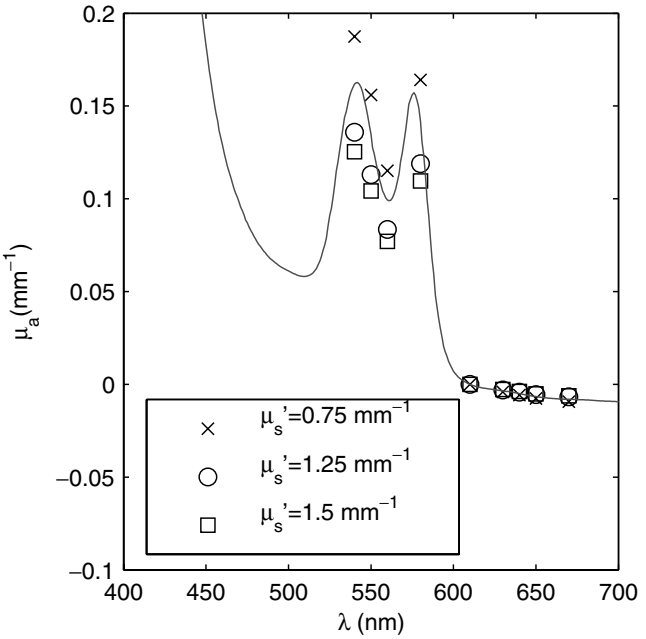

Fig. 14. Comparison of the measured (symbol) and expected (solid) absorption coefficient versus wavelength for the three liquid phantoms.

where $\mu_a^{\mathrm{Hb\,Oxy}}$ and $\mu_a^{\mathrm{Hb\,Deoxy}}$ are the absorption coefficients of oxy- and deoxy-hemoglobin, respectively. Hence, oxygen saturation can be extracted from the absorption coefficient values.

4. Conclusions

We presented the implementation on a regular fundus ophthalmoscope of a retinal spectroscopic imager and a retina blood flow velocimeter. The retina imaging part of the setup was a snapshot multi-aperture imaging system designed for retinal oxygen saturation measurements. A Zemax-optimized optical train was added to the original ophthalmoscope optics for division of aperture purposes. Nine equivalent wavelength-dependent sub-images of the retina were projected onto a large format CCD. Spectral sensitivity was measured and registration of the nine images was performed using a USAF 1951 test target. A grid of optical phantoms matching the reflectance and the optical properties of the retina was used to calibrate the setup and build a lookup table (LUT). Reflectance values from a set of liquid phantoms, mixing human hemoglobin with polystyrene microspheres, were measured. Analysis with the LUT using a nonlinear fit procedure was performed to extract the absorption and reduced scattering coefficients, with a good agreement to the issued reference

values of a spectroscopic measurement (absorption coefficient) and Mie calculations (reduced scattering coefficient). The blood velocimeter used a green illumination LED-based engine, replacing the original bulb of the fundus camera to increase retina images contrast. The original ophthalmoscope eyepiece was replaced with an imaging system composed of a zoom lens attached to a fast acquisition camera. Calibration with a capillary tube pumped with human blood at a known rate, located at the fundus of an eye phantom, was performed. Results of blood flow in a patient eye were presented.

Acknowledgments

We thank D. Smolley for technical assistance in achieving the mechanical items. We are grateful for the support from the Coulter Foundation and NIH grant #EY017577-01A11.

References

1. N. D. Wangsa-Wirawan, R. A. Linsenmeier, "Retinal oxygen: Fundamental and clinical aspects," *Arch. Ophthalmol.* **121**, 547–557 (2003).
2. Q. D. Nguyen, S. M. Shah, E. V. Anden, J. U. Sung, S. Vitale, P. A. Campochiaro, "Supplemental oxygen improves diabetic macular edema: A pilot study," *Invest. Ophthalmol. Vis. Sci.* **45**, 617–624 (2004).
3. E. Kohner, V. Patel, S. Rassam, "Role of blood flow and impaired autoregulation in the pathogenesis of diabetic retinopathy," *Diabetes* **44**, 603–607 (1995).
4. J. Ramella-Roman, S. Mathews, "Spectroscopic measurements of oxygen saturation in the retina," *IEEE Journal of Selected Topics in Quantum Electronics* **13**, 1697–1703 (2007).
5. W. R. Johnson, D. W. Wilson, W. Fink, G. Humayun, Mark and Bearman, "Snapshot hyperspectral imaging in ophthalmology," *J. Biomed. Opt.* **12**, 014036 (2007).
6. M. Hammer, W. Vilser, T. Riemer, D. Schweitzer, "Retinal vessel oximetry-calibration, compensation for vessel diameter and fundus pigmentation, and reproducibility," *J. Biomed. Opt.* **13**, 054015 (2008).
7. S. H. Hardarson, M. S. Gottfredsdottir, G. H. Halldorsson, R. A. Karlsson, J. A. Benediktsson, T. Eysteinsson, J. M. Beach, A. Harris, E. Stefansson, "Glaucoma filtration surgery and retinal oxygen saturation," *Invest. Ophthalmol. Vis. Sci.* **50**, 5247–5250 (2009).
8. S. H. Hardarson, S. Basit, T. E. Jonsdottir, T. Eysteinsson, G. H. Halldorsson, R. A. Karlsson, J. M. Beach, J. A. Benediktsson, E. Stefansson, "Oxygen saturation in human retinal vessels is higher in dark than in light," *Invest. Ophthalmol. Vis. Sci.* **50**, 2308–2311 (2009).
9. C. E. Riva, "Basic principles of laser Doppler flowmetry and application to the ocular circulation," *Int. Ophthalmol.* **28**, 183–189 (2001).
10. C. E. Riva, B. L. Petrig, R. D. Shonat, C. J. Pournaras, "Scattering process in ldv from retinal vessels," *Appl. Opt.* **28**, 1078–1083 (1989).
11. M. J. Mendel, V. V. Toi, C. E. Riva, B. L. Petrig, "Eye-tracking laser Doppler velocimeter stabilized in two dimensions: Principle, design, and construction," *J. Opt. Soc. Am. A* **10**, 1663–1669 (1993).
12. N. Konishi, H. Fujii, "Real-time visualization of retinal microcirculation by laser flowgraphy," *Opt. Eng.* **34**, 753–757 (1995).
13. H. Cheng, Y. Yan, T. Q. Duong, "Temporal statistical analysis of laser speckle images and its application to retinal blood-flow imaging," *Opt. Express* **16**, 10214–10219 (2008).
14. D. D. Duncan, S. J. Kirkpatrick, "Can laser speckle flowmetry be made a quantitative tool?" *J. Opt. Soc. Am. A* **25**, 2088–2094 (2008).
15. P. Lemaillet, J. C. Ramella-Roman, "Dynamic eye phantom for retinal oximetry measurements," *J. Biomed. Opt.* **14**, 064008 (2009).
16. M. Hammer, A. Roggan, D. Schweitzer, G. Müller, "Optical properties of ocular fundus tissues — An *in vitro* study using the double-integrating-sphere technique and inverse Monte Carlo simulation," *Phys. Med. Biol.* **40**, 963–978 (1995).
17. S. J. Preece, E. Claridge, "Monte Carlo modelling of the spectral reflectance of the human eye," *Phys. Med. Biol.* **47**, 2863–2877 (2002).
18. H. M. Sarna, "The physical properties of melanins," in *The Pigmentary System*, R. E. Nordlund, V. J. Hearing, R. A. King, J. P. Ortonne, eds., Oxford University Press, pp. 439–450 (1998).
19. J. M. Fitts, "Precision correlation tracking via optimal weighting functions," **18**, 280–283 (1979).
20. L. Stephan, J. E. Albus, J. R. Marcovici, "Fitts correlation tracker fidelity in presence of target translation, rotation, and size change," *SPIE* **4714**, 196–207 (2002).
21. S. Wong, "Advanced correlation tracking of objects in cluttered imagery," *SPIE* **5810**, 158–169 (2005).
22. D. D. Duncan, P. Lemaillet, M. Ibrahim, Q. D. Nguyen, M. Hiller, J. C. Ramella-Roman, "Absolute blood velocity measured with a modified fundus camera," *J. Biomed. Opt.*, to be published.
23. T. Moffitt, Y.-C. Chen, S. A. Prahl, "Preparation and characterization of polyurethane optical phantoms," *J. Biomed. Opt.* **11**, 041103 (2006).
24. S. A. Prahl, "The adding-doubling method," in *Optical-Thermal Response of Laser Irradiated*

Tissue, A. J. Welch, M. J. C. van Gemert, eds. Plenum Press, Chap. 5, pp. 101–129 (1995).

25. L. Wang, S. L. Jacques, L. Zheng, "Mcml–Monte Carlo modeling of light transport in multilayered tissues," *Computer Meth. Prog. Biomed.* **47**, 131–146 (1995).
26. N. Rajaram, T. H. Nguyen, J. W. Tunnell, "Lookup table-based inverse model for determining optical properties of turbid media," *J. Biomed. Opt.* **13**, 050501 (2008).